

Three-Dimensional Design and Optimization of the Liquid Cooling System for the FITGEN E-Axle

Abstract

The H2020 funded FITGEN project aims to deliver a fully integrated e-motor-inverter-transmission power unit for next generation electric vehicles. This paper describes the design and optimization of a liquid cooling system for the e-motor. Three variants of a three-dimensional conjugate heat transfer model, based on the Reynolds-averaged Navier-Stokes (RANS) and energy equations, are used to carry out the design process: a CFD model of the liquid cooling system to assess candidate configurations, a CFD and heat transfer model of the full e-motor to calculate heat transfer boundary conditions, and a CFD and heat transfer model of a reduced geometry including liquid cooling system to carry out optimization and sensitivity studies. The design process identifies a promising cooling system configuration made up of axial and circumferential ribs, satisfying requirements for inlet and outlet position, volumetric flow rate, overall pressure drop, manufacturability and maintainability. An optimization study is carried out on the size of a mandatory gap, between the ribs and the outer part of the e-motor external housing, through which coolant is allowed to flow. Sensitivity studies are carried out to assess the effect of off-design variation in the aforementioned gap and the rib width. The results provide insight into the fluid dynamic and thermal behaviour of the cooling system, the optimal sizing of the rib-outer housing gap, and the effect of off-design variation on temperature and pressure drop. A design for the liquid cooling system is proposed.

Introduction

The H2020 funded FITGEN project aims to deliver a fully integrated e-motor-inverter-transmission power unit, also referred to as an e-axle, for next generation electric vehicles. The three main components are a 6-phase inverter, a high-speed 6-phase buried permanent magnet e-motor, and a single speed transmission as shown in Figure 1. It delivers 135kW peak power with high compactness and low weight due to a highly integrated common housing for the inverter and the e-motor. This housing features a liquid cooling system for both the inverter and the e-motor.

The primary target vehicle, for which the e-axle will be validated, is an A-segment battery electric vehicle. However, the machine has also been designed to be suitable for a small SUV segment plug-in hybrid electric vehicle, and a large SUV segment battery electric vehicle. The performance specifications for the A-segment vehicle are a maximum speed of 160 km/h and acceleration time of 10 s from 0-100 km/h at zero gradient, a maximum gradient of 30% with 0.05g acceleration from standstill a maximum speed of 10 km/h, and a maximum gradient of 5% at 100 km/h. These specifications for the small and large SUV vehicles are 130 km/h, 12 s, 30% and 5%, and 220 km/h, 7 s, 45% and 5%, respectively. The performance characteristics have been used along with the Worldwide Harmonized Light Vehicle Test Procedure Class 3b to derive detailed high level

specifications for the power electronics, e-motor and transmission architecture and interfaces.

One of the main developmental trends in the quest for more efficient electric vehicles is the increase in volumetric power density delivered by the power train. With the associated increase in volumetric density of the heat producing losses and reduction in available surface area for cooling systems, the ability to keep maximum temperatures in key components over the whole operating range is a limiting factor which is becoming increasingly challenging to manage. Two key components in this respect are the winding insulation and the magnets. Spatial variation in the three-dimensional temperature fields in these components can be significant. Effective thermal management of potential hotspots requires sufficient local coolant flow, which depends upon the three-dimensional flow field. The FITGEN e-motor therefore requires an efficient, robust liquid cooling system within its external housing, designed in three-dimensions.

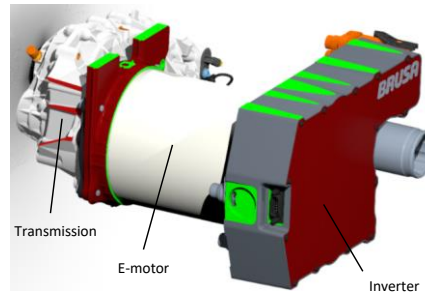


Figure 1. 3D CAD model of the FITGEN e-axle showing the integrated e-motor, inverter and transmission.

Available literature on the topic of e-motor cooling systems focusses on the calculation of specific design cases using numerical models, for example, Huang *et al.* [1], Li *et al.* [2], Kumar *et al.* [3], Pechanek *et al.* [4], and De Gennaro *et al.* [5], or on approaches to modelling specific aspects of e-motor thermal models, for example, Staton *et al.* [6], Yang *et al.* [7], Hosain *et al.* [8] and Wrobel *et al.* [9]. The main relevance of these pieces of work to the FITGEN liquid cooling system are in the design approaches and details of the computational models. A recent review of the state of the art of electric traction motor cooling techniques was provided by Carriero *et al.* [10]. The review outlines the configurations, advantages and drawbacks of an array of the latest approaches to electric motor cooling, namely use of conductive resins, open loop air forced cooling, closed loop air forced cooling, outer jacket liquid cooling, hollow shaft liquid cooling, hollow shaft and stator liquid cooling, hollow shaft stator and gearbox liquid cooling, rotor and stator oil cooling, and rotor and stator oil spray cooling. In FITGEN, the use of the outer jacket liquid

Commented [DGM1]: I believe this is a peak power, right?

cooling system type has been determined and in this paper is assumed so that focus may be cast on the detailed design.

A design process has been carried out to develop a cooling system for the e-motor in its part of the housing which has a length and radius of approximately 310 mm and 100 mm respectively. This paper gives a detailed overview of the three-dimensional computational conjugate heat transfer model used for the design process, design strategy, conjugate heat transfer calculation results, analysis and design proposal, where requirements for specific inlet and outlet position, structural integrity, manufacturability and maintainability are met while simultaneously optimizing the fluid dynamics and heat management. The design analysis focusses on the following factors: even distribution of coolant flow throughout the cooling system domain, the effect of a mandatory gap between the cooling system ribs on the inner housing and the outer housing, and the effect of rib width. Both design optimization and off-design sensitivity are considered.

Methodology

To enable the design of the cooling system, a three-dimensional computational model of the fluid dynamics and heat transfer in the cooling channel, motor and immediate surroundings has been developed. The full geometry available for the model comprises the rotor, air gap surrounding the rotor, stator, bearing plate, external housing, and an annular volume within the external housing where the cooling system is located. The rotor comprises the shaft, rotor iron, balancing disks and magnets. The stator comprises the winding, stator iron and potting. The external housing comprises an inner and outer housing which, together, fully encase the liquid cooling system. The cooling system is part of a global cooling circuit traversing the DC/DC converter, the AC/DC inverter and the e-motor. However, in this model only the part traversing the e-motor, contained within the housing including the inlet and outlet, is considered. The list of model parts and their respective materials is shown in Table 1.

Table 1. List of model parts and their respective materials.

Part / Region	Material
Magnets	NdFeB (Neodym-Iron-Boron)
Rotor iron	Electric Steel NO27
Shaft	Tempered steel
Balancing disks	Stainless steel
Air gap	Air at 94°C
Winding	Copper
Stator	Electric Steel NO27
Potting	Epoxy Resin
Bearing plate	Aluminium
Inner housing	Aluminium
Outer housing	Aluminium
External air	Air at 65°C
Liquid coolant	Water-glycol 50:50 mixture

Three variants of the model have been created:

1.
- The first variant considers only the fluid dynamics in the liquid cooling system, without heat transfer, for initial assessment of the cooling system flow distribution.

2.
- The second variant considers the fluid dynamics and heat transfer in the entire e-motor geometry and the external surroundings, in order to calculate heat flux, heat transfer coefficient and temperature boundary conditions for the third variant.
3.
- The third variant is a reduction of the second, considering the fluid dynamics and heat transfer in the stator, bearing plate and liquid cooling system, and is used to carry out the design optimization and sensitivity studies.

The solver used is ANSYS Fluent. As the Reynolds number for the rotor-stator air gap is of order 10^3 and for the coolant channel is expected to be in the upper reaches of 2,600 – 10,000 or greater, the flow is solved using the steady Reynolds-averaged Navier-Stokes (RANS) equations with the k-omega SST turbulence model with fully resolved boundary layers. The heat transfer is solved using the steady energy equation.

Variant 1: Liquid Cooling System Fluid Dynamics Only

The first variant comprises the liquid cooling system. Figure 2 shows a sample geometry. Only the RANS equations are solved with this variant, without the energy equation. A velocity condition prescribing a volumetric flow rate of 8 litres/min is applied at the inlet, a pressure condition is applied at the outlet, and the no-slip condition on all solid boundaries.

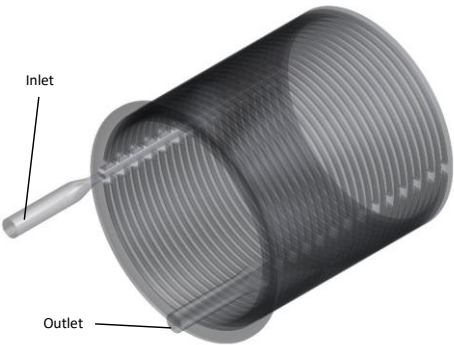


Figure 2. Example liquid cooling system geometry for model variant 1.

The mesh consists of polyhedral elements with inflation layers on all solid boundaries. The cell resolution has been set to provide y-plus values of approximately one, delivering full boundary layer resolution without the use of wall functions. A mesh invariance study was carried out to ensure the convergence of the velocity field and overall pressure drop.

Variant 2: Full E-motor Fluid Dynamics and Energy

The second variant comprises the rotor, air gap, stator, bearing plate, external housing, liquid cooling system, and an idealized fluid volume representing the external air space around the motor. Figure 3 shows the geometry.

Commented [DGM2]: This sentence is not needed.

Commented [PJ3]: Note to self: consider wording.

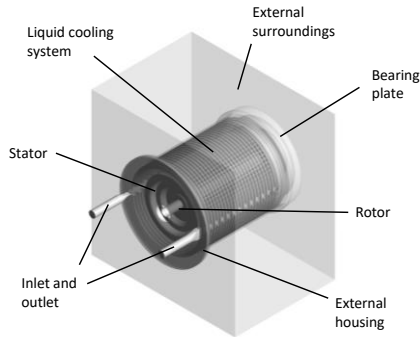


Figure 3. Geometry of the second variant of the computational model, including the rotor, air gap, stator, external housing, liquid cooling system and external surroundings.

The power losses of the magnets, rotor iron, winding and stator iron are applied evenly distributed throughout their respective volumes in the model. The velocity field of the rotor surface is applied to the corresponding surface in the air gap domain to generate the Taylor-Couette flow between the rotor and stator in the air gap and the air motion around the balancing disks and shaft. At 22,500 rpm with a radius of 58.5 mm, the velocity on the rotor iron surface in the 0.5 mm air gap is 137.8 m/s. The Taylor number in the gap is of the order of 10^5 which is well into the region of fully turbulent Taylor-Couette flow.

The fluid boundary conditions for the liquid cooling system are as in variant 1. The inlet temperature for the cooling system is set to the specified outside air temperature plus 5°C to account for the upstream temperature rise in the global cooling system. An idealized shear flow is imposed in the lower part of the external surrounding air space with an inlet temperature equal to the specified outside air temperature. The no-slip condition is applied on all solid boundaries in the fluid domains. Due to insufficient data on the thermal behaviour of the inverter and gear box in the fully integrated e-axle and wider surrounding area at the time of development, all boundaries with the inverter and gearbox, and at the limit of the external surroundings are considered adiabatic, and there is no consideration of radiative heat transfer in the model.

The mesh consists of hexahedral cells in the rotor iron, magnets and thin annular part of the air gap, and tetrahedral cells in the remainder of the model. The cell resolution has been set in the air gap and the inflation layers used elsewhere in the fluid domains to provide y-plus values of approximately one. Full boundary layer resolution without wall functions is applied on these boundaries. On the outermost solid boundary in the external surroundings no inflation is used as the flow field here is far from the area of interest. Therefore wall functions are applied here. A mesh invariance study was carried out to ensure the convergence of the heat flux fields on the stator inner surface and external housing outer surface. The total cell count in the variant is 120 million cells.

Variant 3: Reduced E-motor Fluid Dynamics and Energy

The third variant comprises the stator, the bearing plate, the external housing, and the liquid cooling system. Figure 4 shows the geometry and mesh of the model including the stator, bearing plate, external housing and liquid cooling system.

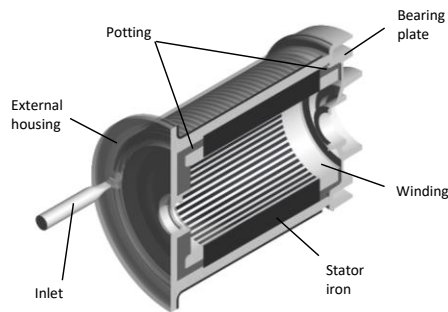


Figure 4. Half of the geometry of the third variant of the computational model, including the stator, bearing plate, external housing and liquid cooling system.

The boundary conditions for variant 3 are unchanged from variant 2 in the parts and boundaries which are common to the two models. The external boundary of the external housing has a heat transfer coefficient and temperature boundary condition applied, which is calculated from the results of variant 2 and surface averaged. The inner boundaries of the stator, bearing plate and external housing have the spatially accurate heat flux surface fields from variant 2 interpolated onto their respective surface meshes.

The mesh consists of polyhedral cells throughout the domain. The cell resolution was controlled in the fluid domain to provide y-plus values of approximately one. Full boundary layer resolution without wall functions is applied on these boundaries. A mesh invariance study was carried out to ensure convergence of the maximum solid component temperatures. The total cell count varied over multiple design iterations between 50 million and 70 million cells. Figure 5 shows a cross-section of the mesh in the stator and liquid cooling system with the polyhedral cells and inflation layers visible.

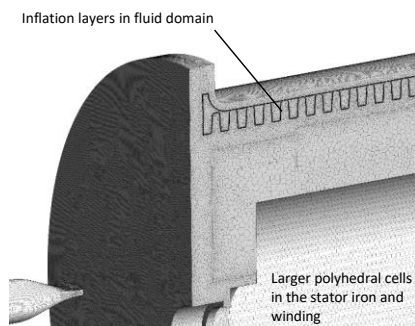


Figure 5. Stator, external housing and liquid cooling system mesh cross-section, showing polyhedral cells and inflation layers.

Design Specifications

Operating conditions

For FITGEN, the range of reference operating conditions for the power train are defined as shown in Table 2. The continuous operating conditions are intended to be maintainable in steady state. The peak operating conditions are intended to be applied for 30 seconds. The losses in the table were calculated for a single e-motor speed for a full range of stator current amplitudes and angles using the finite element software ANSYS Maxwell. The results of the calculation were stored in lookup tables, which were then used for interpolation along with either maximum torque per ampere (MTPA) or field weakening control to estimate the losses for the specified torque values and voltage constraints. The losses were then scaled using the ratio of actual machine speed to simulated speed. While the losses were calculated per component and applied as such in the calculations in this paper, the exact split between stator iron and copper and between rotor iron and magnets is not disclosed.

Table 2. Reference operating conditions for the e-motor. The numbers represent continuous / peak operation.

Speed (rpm)	Torque (Nm)	Stator iron and copper losses (kW)	Rotor iron and magnet losses (kW)
7,500	80.0 / 173.4	2.10000 / 5.23000	0.14054 / 0.29171
15,000	44.4 / 86.3	2.19000 / 6.01000	0.22161 / 0.58765
22,500	29.7 / 57.3	2.89000 / 9.06000	0.27422 / 1.01934

The operational outside air temperature range is defined as -40°C to +65°C. For the design and optimization of the liquid cooling system, the continuous operating condition at 22,500 rpm was selected, along with an outside air temperature of +65°C, as it represents the most challenging thermal conditions intended to be applied for a significant amount of time. Peak operating conditions were not considered for optimization due to their highly transient nature. The volumetric flow rate of the coolant was specified by the project

partners to be 8 litres per minute and the overall pressure drop for the e-motor section of the cooling system to not exceed 17 kPa.

Geometric Constraints

The FITGEN e-axle has been designed for a high level of integration between the main components, low weight, ease of manufacturability, ease of maintainability and durability, leading to a number of key geometric constraints on the design. The use of a common external housing for the e-motor and inverter, combined with the common global cooling system for both requires that the inlet and outlet both be located at the inverter end of the motor. This eliminates configurations such as the helix from candidacy. The design of the housing for low weight and ease of maintenance has resulted in it featuring a separate outer housing, attached via welding and bolts with a seal. This part is of the form of a thin tube of limited rigidity. The ribs are therefore attached to (effectively part of) the inner housing. The manufacturing variation of the outer housing inner diameter is great enough that a gap is required between the ribs and the outer housing on design to ensure off-design robustness. The design of the housing, to be suitable for sand or die casting without excessive extra machining, requires the ribs to be compatible with the casting process. As a casted model could always have some blowholes, a minimum thickness of 3 mm at the top of the rib is required. To demould the cast component, the side walls of the ribs should also have an angle of at least 3° to the casting axis.

Figure 6 shows a half-section of the housing including cross-sections of sample ribs and coolant channels. The inner and outer housing are clearly visible. The presence and form of the rib-outer housing gap and an end gap can be clearly appreciated. The former allows coolant to flow from one channel to the other without following the labyrinth and the latter offers a direct channel from inlet to outlet, which bypasses the labyrinth.

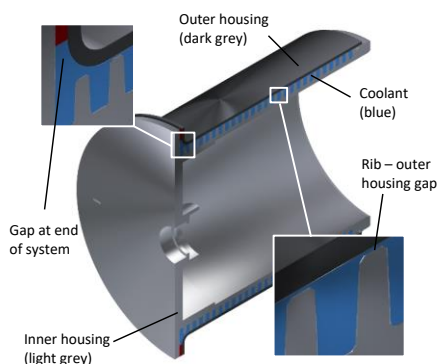


Figure 6. External housing half-section showing the inner and outer housing, cross-sections of the ribs and coolant channels, and highlighting the rib-outer housing gap and the end gap.

Design Process

The design process consists of four overall steps:

1. Model variant 1 is used to calculate the flow in candidate cooling system configurations in order to eliminate those with flow fields which exhibit poor coverage of the available volume.
2. Model variant 1 is used to find the values of key parameters of the promising configuration(s) which deliver an overall system pressure drop of 17 kPa. This is typically the number of ribs, which sets the channel widths and overall length of the labyrinth.
3. Model variant 2 is used to calculate the RANS and energy equation solution in the full domain and the thermal boundary conditions were extracted for model variant 2.
4. Model variant 3 is used to carry out optimization and sensitivity studies on further key parameters of the promising configuration(s).

Calculation Results

Variant 1 CFD only results

The results of the RANS calculations of the candidate configurations using model variant 1 will for brevity be sketched. Not all conceivable configurations were considered as the first few candidates showed fluid behavior which ruled out a side by side inlet and outlet and prioritized channeling flow to the opposite end of the machine to the outlet. The results for the only candidate which was considered suitable for the full design process will be shown later in more detail.

The first candidate was characterized by the inlet and outlet being located adjacent to each other and an axial back and forth channel labyrinth. Figure 7 shows a sketch of the main trend in the flow field. The presence of the rib-outer housing gap combined with the proximity of the inlet and outlet induced a significant pressure gradient across the gap and a corresponding large volume flux. This was further compounded by the need to bunch up the ribs in order to permit die casting. The wide channel leading from the inlet had a low rate which permitted a greater flow across the gap than if the channel had been narrow with a high flow rate. This effect can be explained by referring to Bernoulli's equation

$$p + \frac{1}{2} \rho v^2 = \text{constant},$$

which states that high velocity corresponds to low pressure and *vice versa*. This effect will be shown to be important later in this paper. The message delivered by this candidate was that the inlet and outlet must be positioned 180° apart around the circumference in order to distribute flow fully around the circumference.

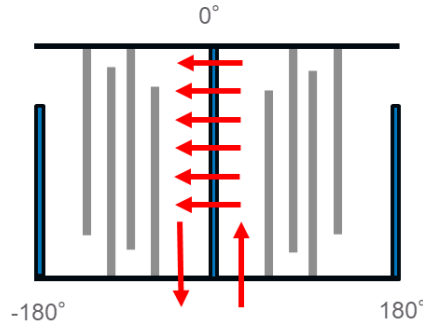


Figure 7. Sketch of the main flow trend in the first candidate configuration.

The second candidate had the inlet and outlet positioned 180° apart at opposite sides of the circumference. Figure 8 shows a sketch of the main flow trend in the second candidate configuration. Here the flow returned to the inverter end of the motor after one axial back and forth with significant flow across the gap and then continued to flow across the gaps around the circumference and through the end gap using the shortest route to the outlet. The message from this candidate was that in addition to a 180° separation of the inlet and outlet, it is necessary to channel the flow immediately to the gearbox end of the motor before distributing it around the circumference.

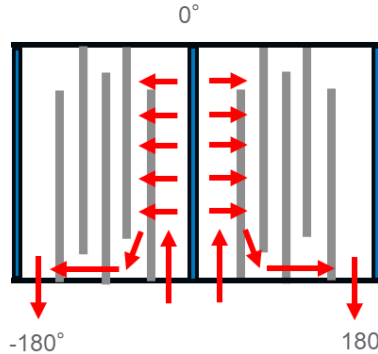


Figure 8. Sketch of the main flow trend in the second candidate configuration.

The third candidate features both the inlet and outlet positioned 180° apart and an axial channel immediately downstream of the inlet to channel the flow to the opposite end of the system. Figure 9 shows a sketch of the configuration and Figure 10 shows streamlines from a steady RANS calculation superimposed on the inner housing for context. The green colour of the streamlines in the axial channel immediately downstream of the inlet and the light blue colour in the first circumferential channels following the axial, both highlighted by the red arrows, show the relatively high velocity of the flow here, inducing low pressure according to Bernoulli's equation and therefore locally minimizing flow in the rib-outer housing gaps. The flow divides at the T-junction at the end of the axial channel (at the right hand end of the system as viewed in Figure 10) and is directed

around the circumference in the first circumferential channel. The remainder of the flow downstream is a combination of circumferential back and forth flow and rib-outer housing gap flow, as highlighted by the black and white arrows respectively.

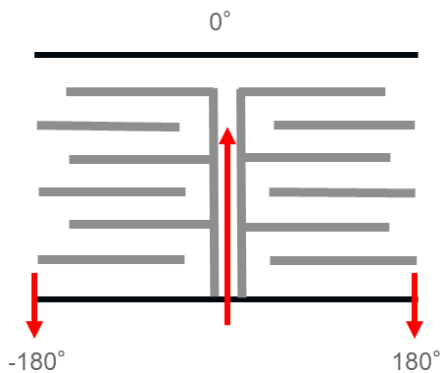


Figure 9. Sketch of the third candidate configuration with the inlet and outlet flows highlighted in red.

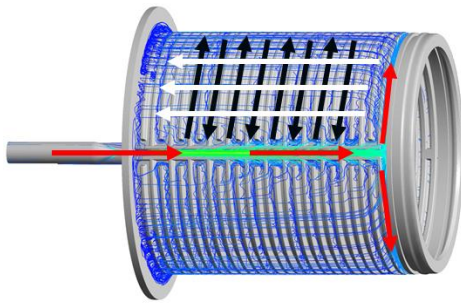


Figure 10. Streamlines coloured by velocity for the third candidate configuration with arrows added to highlight the main flow mechanisms.

The third candidate configuration achieves a promising delivery of coolant to the right hand end of the system and, in turn, of flow around the circumference at the same end. This provides the most satisfactory distribution of flow throughout the axial and circumferential extents of the available domain. This is in stark contrast to the insufficient circumferential flow distribution in the first candidate and axial flow distribution in the second. This configuration was selected for the design and the number of circumferential channels was set to 27 to give an overall pressure drop of approximately 17 kPa for the next stage of the design process. All of the studies presented in this paper from here onwards are based on this setup.

Variant 2 CFD and Energy Equation Results

The results provided by variant 2 include a shear flow in the external surroundings along with associated air motion around the e-motor to represent the effect of the vehicle motion, a Taylor-Couette flow in the air gap between the rotor and stator along with the rotating air flow in the same air space at either end of the rotor, a full liquid coolant flow field and temperature and heat flux solutions throughout the solid and fluid domain. No significant asymmetry in the temperature field or extracted heat flux boundary conditions due to the frozen rotor approach combined with the rotationally non-symmetric liquid cooling system was noticed. As this variant was only used to calculate boundary conditions for variant 3, no results will be shown or discussed here.

Variant 3 Design Results and Analysis

The following studies were carried out using the model variant 3 to further optimize the geometry from the starting point of outcome of the variant 1 studies which provided an overall configuration calibrated to deliver an overall pressure drop of 17 kPa.

A parametric study on the effect of rib-outer cover gap on the heat transfer between the motor and the liquid coolant and in particular on the maximum temperature in the winding has been carried out. Figure 11 shows the variation of the maximum winding temperature with the magnitude of the rib-outer housing gap. The results have the dual purpose of calculating the optimum magnitude of the gap for cooling efficiency and demonstrating the sensitivity of the maximum winding temperature to manufacturing variation in the gap magnitude. A minimum in the temperature can be clearly seen in the vicinity of 0.6 mm which indicates the optimum. The gradient between 0.0 mm and 0.2 mm is relatively steep, indicating that an off-design gap in this range is undesirable. However, off-design gap variation above 0.2 mm has comparatively insignificant consequences from a thermal management point of view.

A parametric study on the effect of rib-outer cover gap on the overall pressure drop in the system has also been carried out. The purpose of the study was to assess the sensitivity of the pressure drop to manufacturing variation in the gap magnitude. Figure 11 shows the variation of the overall pressure drop with the gap magnitude. Between 0.2 mm and 1.0 mm the variation in pressure drop is inverse and approximately linear, with a relatively moderate variation between 15.2 kPa and 18.2 kPa. Between 0.2 mm and 0.0 mm the pressure drop rises significantly to 24.8 kPa. The flow mechanisms responsible for the sharp increase are, at the time of writing, under continued investigation. These results suggest that the minimum allowed gap magnitude under manufacturing variation should be no less than 0.2 mm, otherwise the design pressure drop would have to be set significantly below 17 kPa. The optimum design gap magnitude of 0.6mm and maximum expected variation of ± 0.4 mm coincide nicely to allow on-design at the optimum value for heat transfer with an off-design expected range of 0.2 mm to 1.0 mm which maintains reasonable performance in terms of both heat transfer and pressure drop.

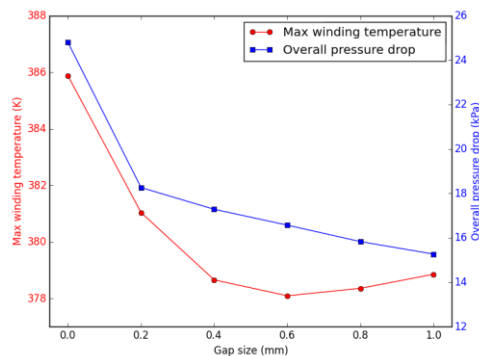


Figure 11. Maximum temperature in the winding and overall system pressure drop versus the magnitude of the rib-outer cover gap.

The effect of the rib-outer housing gap on maximum winding temperature seems not intuitive and with a temperature range of almost 8 K is of some significance from a thermal management point of view. Figure 12 shows the pressure contours for the rib-outer housing gap of 0.6 mm, at a mid radial height in the liquid cooling system, viewed from the inlet side. Figure 13 to Figure 18 show the surface temperature contours for the inner housing, for rib-outer housing gaps of 0.2 mm, 0.6 mm and 1.0 mm, viewed from the inlet side and outlet side. The number of circumferential channels is constant across the three cases, giving pressure drops of approximately 17 kPa. The rib width is 3 mm for all three cases.

In each of the three cases there is a common overall pattern. Figure 14 is referred to in the following description. On the inlet side, the coolest part of the housing surface coincides with the axial channel and the 'T-junction' with the first circumferential channel at the right hand end of the domain. Immediately downstream of the inlet, the flow in the axial channel behaves as a jet. Here, the local pressure is lower than in the adjacent circumferential channels. The circumferential cool band (1) in the adjacent circumferential channels suggests this pressure system has a favourable effect here. In the rest of the axial channel, further downstream, the local pressure becomes increasing greater than that in the adjacent circumferential channels. This drives a 'leakage' flow through the rib-outer cover gap from the axial channel to the circumferential channels. This appears to have a local cooling effect (2) in the circumferential channels but, beyond that, warm regions (3) can also be observed, which suggests the leakage out of the axial channel may have a detrimental effect beyond the local cooling it provides. On the outlet side, the cool band at the left hand end and the warm patches in the mid-section are seen to persist around the circumference. There is, however, a warm patch (4) at the right hand end shows that the coolant flow does not reach the end of the first circumferential channel with enough momentum, possibly weakened by the leakage flow.

With the commonalities as a base line, the 1.0 mm and 0.2 mm cases can now be compared in turn to the 0.6 mm case. The 1.0 mm gap provides less resistance to leakage flow than the 0.6 mm gap, which provides a greater possibility for interaction between the axial channel flow and the circumferential. Comparing Figure 14 with

Figure 15 and Figure 17 with Figure 18 it can be observed that the pattern in the inner housing temperature contours is broadly similar but with increased temperature visible over most of the surface in the 1.0 mm case. This suggests that there is little fundamental change in the overall flow pattern of the coolant, but the importance of the leakage flow relative to the channel flow has increased past its optimum.

The 0.2 mm gap provides a greater resistance to leakage flow, which results in less interaction of the axial channel flow with the circumferential. Comparing Figure 13 with Figure 14 and Figure 16 with Figure 17 it be seen that this leads to increased cooling at the left hand end immediately downstream of the inlet, but also reduced cooling at the right hand end. The warm patches in the circumferential channels are positioned further towards the right hand side and are more profound, in line with the reduced leakage flow along the axial channel. The difference with the greatest significance with respect to thermal management, however, is the increased temperature visible in Figure 16 at the right hand end on the outlet side of the housing, which shows that the coolant flow is less effective at reaching this area furthest in the system from the inlet. Reaching this region represents the main design challenge for this type of system.

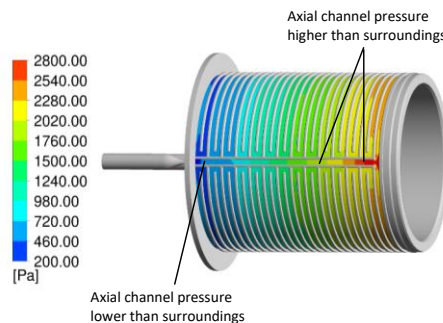


Figure 12. Pressure contours in the liquid cooling system, for the case with a 0.2 mm gap, viewed at a mid radial height.

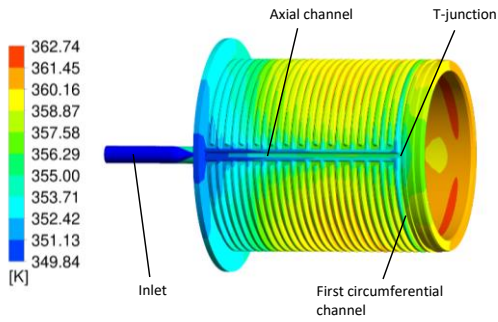


Figure 13. Surface temperature contours for the inner housing, for the case with a 0.2mm gap, viewed from the inlet side.

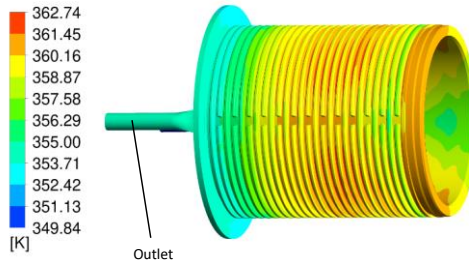


Figure 16. Surface temperature contours for the inner housing, for the case with a 0.2mm gap, viewed from the outlet side.

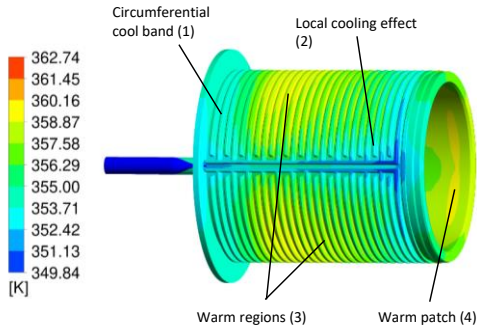


Figure 14. Surface temperature contours for the inner housing, for the case with a 0.6mm gap, viewed from the inlet side.

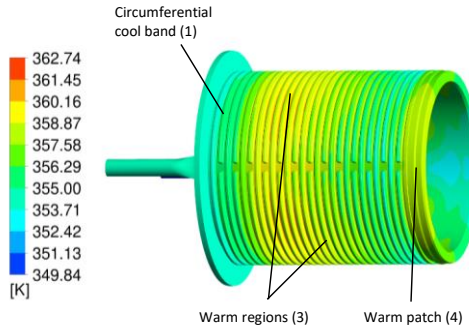


Figure 17. Surface temperature contours for the inner housing, for the case with a 0.6mm gap, viewed from the outlet side.

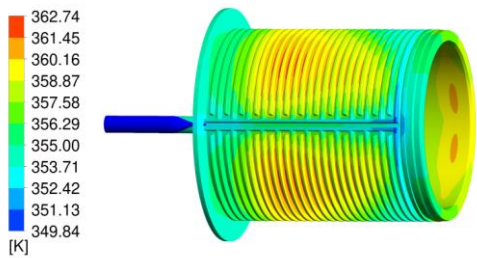


Figure 15. Surface temperature contours for the inner housing, for the case with a 1.0mm gap, viewed from the inlet side.

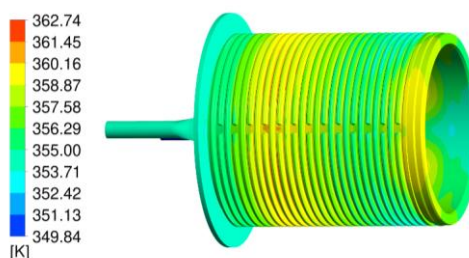


Figure 18. Surface temperature contours for the inner housing, for the case with a 1.0mm gap, viewed from the outlet side.

To correlate the spatial cooling effects of the liquid coolant on the inner housing with our objective of reducing the maximum temperature in the copper winding, the temperature contours on the winding surface are shown in Figure 19 and Figure 20, viewed from the inlet side and the outlet side respectively. The first key observation is the contours on the inlet show the lowest temperatures at a particular axial location coinciding well with the circumferential position of the axial channel. The second is that the contours on both figures show the lowest temperatures at a particular circumferential location appear in the mid-section of the winding and the highest temperatures on both the left and right hand side. These variations combine to give two hot spots, one at each end, 180° circumferentially around from the axial channel. This further demonstrates the importance of improving the coolant flow to the end of the first circumferential channel on the right hand side.

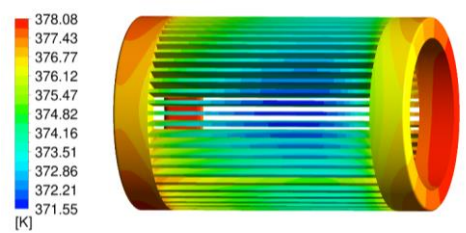


Figure 19. Surface temperature contours for the copper winding, viewed from the inlet side.

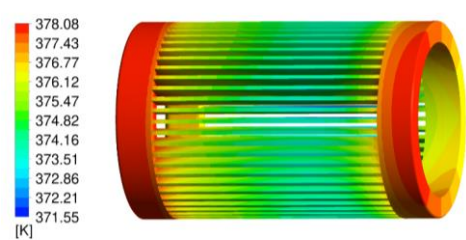


Figure 20. Surface temperature contours for the copper winding, viewed from the outlet side.

A parametric study on the effect of rib width on the heat transfer between the motor and the liquid coolant and in particular on the maximum temperature in the winding has also been carried out. The number of circumferential channels is fixed so as the rib width

increases, the channel width decreases. The purpose of the study is to assess the sensitivity of the cooling performance to manufacturing variation. Figure 21 shows the variation of the maximum winding temperature with the rib width. The temperature decreases by just over 3 K as the rib width increases from 2 mm to 4 mm. Considering the extent of the rib width variation, the change in temperature can be considered small. Two possible reasons for the effect are the increased fluid velocity in the narrower channels leading to increased turbulent mixing of the thermal boundary layer with the main flow and the increased resistance to flow through the rib-outer cover channel. Based on this study, it was decided not to invest in investigating wider ribs with a reduced number of circumferential channels to maintain a pressure drop of 17 kPa. It is likely that reducing the number of channels will have a more significant upward influence on the temperatures than the downward influence of widening the ribs.

Finally, a parametric study on the effect of rib width on the overall pressure drop has been carried out. Figure 21 shows the variation of the pressure drop with the rib width. Contrary to the previous equivalent results for maximum winding temperature, the effect shown in the plot on pressure is considerable. Between 2 mm and 3 mm, the pressure drop almost doubles and from 3 mm to 4 mm it rises by a factor of over 2.5. The results show the potential for large variation in off-design pressure drop, to which there are a number of possible solutions including: utilizing a high manufacturing precision, designing in large buffer in the on-design pressure drop, or increasing the rib width to proportionately reduce the manufacturing variation and accordingly reducing the number of channels to maintain the pressure drop.

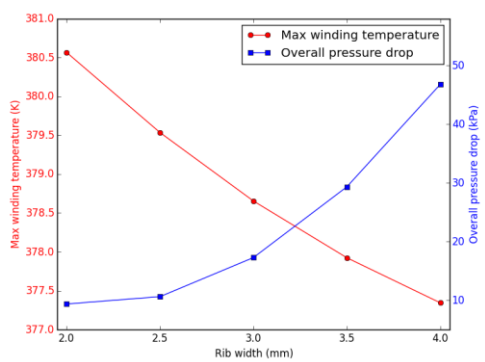


Figure 21. Maximum temperature in the winding and overall system pressure drop versus the rib width.

Conclusions

In this paper, the design challenge presented by the FITGEN e-motor liquid cooling system has been introduced, the development of a comprehensive 3D conjugate heat transfer model has been described in detail, the separation of the model into three variants for use in different stages of the design process has been described, the design process has been outlined and, finally, the results of the design

optimization and sensitivity studies have been presented and analyzed.

The key understanding provided by this research is, firstly, that a rib-outer cover gap, or equivalent depending on specifics other cooling systems, is potentially desirable for heat transfer. This is a result which is perhaps non-intuitive or even counter intuitive to some designers. Secondly, for the FITGEN e-motor, the optimum gap magnitude has been calculated with respect to both optimum maximum winding temperature on design and pressure drop variation off design. Thirdly, manufacturing variation is of little consequence with respect to heat transfer but highly significant consequence to off-design variation in the overall system pressure drop. This poses the important question of how to mitigate such variation. In the event that a range of the rib width manufacturing variation or even a probability density function can be specified, a buffer for the pressure drop can be designed into the system or further rib width-channel number trade-off design studies can be carried out to minimize this effect.

Based on the work presented in this paper, a design for the FITGEN liquid cooling system has been proposed with a 17 kPa on-design pressure drop, 3 mm wide ribs and the optimum rib-outer cover gap of 0.6 mm.

Future Design Optimization and Research

Current and future research into design and optimization methods applicable to this design study are and will be the exploration of automatic optimization methods, including adjoint optimization, as tools to further improve the design of this cooling system and develop more effective and potentially more exotic designs.

The analyses of pressure drop sensitivity to off-design variation in rib width poses interesting questions as to the need and how to increase the robustness of the design with respect to large scale manufacturing. More powerful uncertainty quantification to propagate detailed manufacturing uncertainty through the design process is under consideration.

References

1. Huang, J., Naini, S. S., Miller, R., Rizzo, D., Sebeck, K., Shurin, S. and Wagner, J. "A Hybrid Electric Vehicle Motor Cooling System— Design, Model, and Control", IEEE Transactions on Vehicular Technology, IEEE, 2019, doi: 10.1109/TVT.2019.2902135.
2. Li, D., Wen, Y., Li, W., Feng, B. and Cao, J., "Three-Dimensional Temperature Field Calculation and Analysis of an Axial-Radial Flux-Type Permanent Magnet Synchronous Motor", Energies, 2018, MDPI.
3. Kumar, A., "Electric Motor Internal Heat Convection Modelling and Analysis", Masters Thesis, 2018, Chalmers University of Technology.
4. Pechanek, R., and Bouzek, L., "Analyzing of Two Types Water Cooling Electric Motors using Computational Fluid Dynamics", EPE-PEMC International Power Electronics and Motion Control Conference, 2012, doi: 10.1109/EPEPEMC.2012.6397424.
5. De Gennaro, M., Juergens, J., Zanon, A., Gragger, J., Schlemmer, E., Fricassè, A., Marengo, L., Ponick, B., Trancho Olabarri, E., Kinder, J., Cavallini, A., Mancinelli, P.,

Page 10 of 10

10/19/2016

- Hernandez, M., Messagie, M., "Designing, prototyping and testing of a ferrite permanent magnet assisted synchronous reluctance machine for hybrid and electric vehicles applications", Journal of Sustainable Energy Technologies and Assessments, Vol. 31, Feb. 2019, pp. 86-101.
6. Staton, D., Boglietti, A., and Cavagnino, A., "Solving the More Difficult Aspects of Electric Motor Thermal Analysis", IEEE International Electric Machines & Drives Conference, Madison, WI, USA, 1-4 June 2003.
 7. Yang, Y., Bilgin, B., Kasprzak, M., Nalakath, S., Sadek, H., Preindl, M., Cotton, J., Schofield, N. and Emadi, A., "Thermal management of electric machines", IET Electrical Systems in Transportation, 2017, 7(2), pp. 104-116, doi: 10.1049/iet-est.2015.0050.
 8. Hosain, M. L., Fdhila, R. B., and Rönnerberg, K., "Air-Gap Flow and Thermal Analysis of Rotating Machines using CFD", ICAE2016, 2016, Elsevier.
 9. Wrobel, R., and Ayat, S., "Analytical Methods for Estimating Equivalent Thermal Conductivity in Impregnated Electrical Windings Formed Using Litz Wire", IEEE International Electric Machines and Drives Conference, 2017, doi: 10.1109/IEMDC.2017.8002003.
 10. Carriero, A., Locatelli, M., Ramakrishnan, K., Mastinu, G., and Gobbi, M., "A Review of the State of the Art of Electric Traction Motors Cooling Techniques", SAE Technical Paper 2018-01-0057, 2018, doi:10.4271/2018-01-0057.

Contact Information

Email Dr. James H. Page: james.page@ait.ac.at

Acknowledgments

The authors are grateful to the European Commission for the support of the present work, performed within the EU H2020 project FITGEN (Grant Agreement 824335).